



# AMERICAN METEOROLOGICAL SOCIETY

*Bulletin of the American Meteorological Society*

## **EARLY ONLINE RELEASE**

This is a preliminary PDF of the author-produced manuscript that has been peer-reviewed and accepted for publication. Since it is being posted so soon after acceptance, it has not yet been copyedited, formatted, or processed by AMS Publications. This preliminary version of the manuscript may be downloaded, distributed, and cited, but please be aware that there will be visual differences and possibly some content differences between this version and the final published version.

The DOI for this manuscript is doi: 10.1175/BAMS-D-15-00235.1

The final published version of this manuscript will replace the preliminary version at the above DOI once it is available.

If you would like to cite this EOR in a separate work, please use the following full citation:

Luo, Y., R. Zhang, Q. Wan, B. Wang, W. Wong, Z. Hu, B. Jou, Y. Lin, R. Johnson, C. Chang, Y. Zhu, X. Zhang, H. Wang, R. Xia, J. Ma, D. Zhang, M. Gao, Y. Zhang, X. Liu, Y. Chen, H. Huang, X. Bao, Z. Ruan, Z. Cui, Z. Meng, J. Sun, M. Wu, H. Wang, X. Peng, W. Qian, K. Zhao, and Y. Xiao, 2016: The Southern China Monsoon Rainfall Experiment (SCMREX). Bull. Amer. Meteor. Soc. doi:10.1175/BAMS-D-15-00235.1, in press.



33  
34  
35  
36  
37  
38  
39  
40  
41  
42  
43  
44  
45  
46  
47  
48  
49  
50  
51  
52  
53  
54  
55  
56  
57  
58  
59

Submitted to *Bulletin of the American Meteorological Society*

(Revised version, 26 August, 2016)

[CAPSULE] A unique program is developed for improving heavy rainfall forecasts over South China during the pre-summer rainy season through field campaigns and research on physical mechanisms and convection-permitting modeling.

[CAPSULE]

Corresponding author address: Dr. Yali Luo, State Key Laboratory of Severe Weather, Chinese Academy of Meteorological Sciences, Beijing 100081, China.  
E-mail: [yali@camsma.cn](mailto:yali@camsma.cn)

60 **Abstract**

61 During the pre-summer rainy season (April-June), South China often experiences  
62 frequent occurrences of extreme rainfall, leading to severe flooding and inundations.  
63 To expedite the efforts in improving the quantitative precipitation forecast (QPF) of  
64 the pre-summer rainy season rainfall, the China Meteorological Administration (CMA)  
65 initiated a nationally coordinated research project, namely, the Southern China  
66 Monsoon Rainfall Experiment (SCMREX) that was endorsed by the World  
67 Meteorological Organization (WMO) as a Research and Development Project (RDP)  
68 of the World Weather Research Programme (WWRP). The SCMREX RDP  
69 (2013-2018) consists of four major components: field campaign, database  
70 management, studies on physical mechanisms of heavy rainfall events, and  
71 convection-permitting numerical experiments including impact of data assimilation,  
72 evaluation/improvement of model physics, and ensemble prediction. The pilot field  
73 campaigns were carried out during early May to mid-June of 2013-15. This paper: (i)  
74 describes the scientific objectives, pilot field campaigns, and data sharing of  
75 SCMREX; (ii) provides an overview of heavy rainfall events during the  
76 SCMREX-2014 intensive observing period; and (iii) presents examples of preliminary  
77 research results and explains future research opportunities.

## 78 **1. Introduction**

79       The pre-summer rainy season (April-June) in South China (Ding 1994),  
80 occurring during the early stage of the East Asian summer monsoon, accounts for  
81 about a half of the annual precipitation amount with maximum seasonal rainfall  
82 accumulation exceeding 800 mm in several areas (Fig. 1). The pre-summer rainy  
83 season in South China reaches its peak frequency of heavy rainfall events and the  
84 maximum daily rainfall amount around the time of the onset of South China Sea (SCS)  
85 monsoon in May (Ding 1994; see Table 3.2 therein). The pre-summer rainy season  
86 ends when the monsoonal rain belt moves northward to the Yangtze River Valley in  
87 central East China in mid-June, when the Meiyu season starts there. Most  
88 precipitation during the pre-summer rainy season is of convective nature with  
89 mesoscale organizational characteristics (Luo et al. 2013; Xia et al. 2015). The  
90 precipitation, mostly taking place hundreds of kilometers ahead (to the south) of a  
91 cold or quasi-stationary front (i.e., in the warm sector), normally has a larger  
92 accumulated rainfall amount than that closely associated with a cold frontal zone  
93 (Huang et al. 1986; Ding 1994).

94       During the pre-summer rainy season, South China and its vicinity often  
95 experience most frequent occurrences of extreme rainfall, leading to severe flooding  
96 and inundations. These storms endanger the safety of lives and cause marked property  
97 damage, often producing devastating economic losses. To improve the scientific  
98 understanding and practical forecast of the pre-summer rainy season rainfall over

99 South China, three research and field programs were conducted in China during  
100 1977-1981 (Huang 1986), 1998 (Zhou 2003), and 2008-2009 (Zhang et al. 2011),  
101 respectively, and their scientific achievements have been summarized by Luo (2016).  
102 However, there are still many unknowns about the mechanisms governing the  
103 formation and evolution of heavy rainfall over South China during the pre-summer  
104 rainy season, especially those related to mesoscale convective systems (MCSs) and  
105 their interactions with larger-scale atmospheric systems, because of the complicated  
106 multi-scale atmospheric processes involved, the complex underlying surface (land/sea  
107 contrast, topography, and urban landscape) (Fig. 1b), and the lack of comprehensive  
108 high-resolution observations. The skills of quantitative precipitation forecast (QPF)  
109 for the extreme rainfall that occurs in the warm sector over South China during the  
110 pre-summer rainy season remain rather low for the global and regional models used at  
111 the National Meteorological Center of China in Beijing and the Regional  
112 Meteorological Center of South China in Guangzhou.

113 To expedite the efforts in improving the QPF during the pre-summer rainy  
114 season in South China, the China Meteorological Administration (CMA) initiated the  
115 nationally coordinated research project, namely, the Southern China Monsoon  
116 Rainfall Experiment (SCMREX) that was endorsed by the World Meteorological  
117 Organization (WMO) in 2012 as a Research and Development Project (RDP) of the  
118 World Weather Research Programme (WWRP). The scientific objectives of the  
119 SCMREX are: (1) to better understand the physical mechanisms governing the  
120 initiation, evolution, morphology, organization, and duration of the

121 heavy-rain-producing MCSs that determine the precise timing and location and  
122 accumulative amount of extreme rainfall; (2) to better understand the microphysical  
123 and kinematic structures of the heavy-rain-producing MCSs that determine the  
124 instantaneous rainfall amount and are of relevance to validating parameterization  
125 schemes representing cloud-precipitation microphysical processes in numerical  
126 weather prediction (NWP) models; and (3) to improve fine-scale QPF skill by better  
127 understanding the multi-scale precipitation processes, assessing the impact of  
128 assimilating high-resolution observations into convection-permitting (horizontal grid  
129 spacing of 1-4 km) numerical models on QPF, and evaluating and improving cloud  
130 microphysical parameterization schemes in convection-permitting models.

131       SCMREX RDP was originally planned to be a 3-year project from 2013 to 2015,  
132 and later extended to 2018 by WMO in October 2015. The RDP consists of four  
133 major components: field campaign, database management, studies on physical  
134 mechanisms of heavy rainfall events, and convection-permitting NWP experiments  
135 including impact of data assimilation, evaluation/improvement of model physics, and  
136 ensemble prediction. The pilot field campaigns were carried out during early May to  
137 mid-June of 2013, 2014, and 2015. A database system has been setup for sharing of  
138 observation data collected from the field campaigns. The data can be accessed  
139 through application online (<http://scmrex.camsma.cn>) where the Implementation  
140 Plan of SCMREX is also available.

## 141 **2. Field Campaign**

142       The field campaign component of SCMREX aims at obtaining composite

143 high-density observations to detect the atmospheric environment and internal  
144 structures of the rainstorms during the pre-summer rainy season of South China. The  
145 intensive observing periods (IOPs) of 2013 covered 15 days (8-17 and 24-28 May  
146 2013), while the IOPs of 2014 and 2015 ran continuously from 1 May to 15 June. The  
147 observing regions covered Guangdong, southeastern Guangxi, Hainan, Hong Kong,  
148 and the offshore of SCS (Fig. 2a). The observing network was built upon the CMA's  
149 operational meteorological observing network consisting of the sounding stations,  
150 Doppler weather radars, wind-profiling radars (WPRs), automated weather stations  
151 (AWSs), Guangdong-Hong Kong-Macau lightning location system (LLS), and  
152 China's Feng-Yun (FY) satellites. The Doppler radars in South China are similar to  
153 the Weather Surveillance Radar-1988 Doppler (WSR-88D) in the United States in  
154 both hardware and software (Zhu and Zhu 2004). A total of seventeen boundary layer  
155 WPRs were deployed along the coastal areas of Guangdong and central Guangdong to  
156 continuously observe the mesoscale wind fields in the planetary boundary layer (PBL)  
157 and the lower troposphere that are of particular importance for studying convective  
158 initiation and development. Seventeen sensors were employed in the  
159 Guangdong-Hong Kong-Macau LLS (Fig. 2b) and the combined magnetic direction  
160 finding (MDF)/time of arrival (TOA) technology was used to detect cloud-to-ground  
161 lightning strike information (Cummins et al. 1998). The flash detection efficiency and  
162 stroke detection efficiency were about 95% and 90%, respectively, and the median  
163 value of location error was estimated to be about 410 m (Zhang et al. 2014). The  
164 FY-2D and FY-2E geostationary satellites generate 28 cloud images in daily basis

165 under normal operation schedule, whereas each of the FY-3A and FY-3B  
166 polar-orbiting satellites collects imager and sounding data over the target area twice a  
167 day. The structures of MCSs, related kinematic or convection characteristics, and  
168 cloud/precipitation microphysical parameters can be inferred not only from the  
169 Doppler radars and the LLS measurements, but also from a series of portable remote  
170 sensing instruments deployed over Guangdong's west coastal region and the Pearl  
171 River Delta area (Fig. 2b). Table 1 lists the major instruments that participated in the  
172 field campaigns.

173 During the SCMREX IOPs in 2013, four sounding stations in Guangdong  
174 Province launched two extra soundings per day (i.e., at 0600 UTC and 1800 UTC) in  
175 addition to the routine observations at 0000 UTC and 1200 UTC. During the 2014 and  
176 2015 IOPs, respectively, five and six sounding stations in Guangdong, Hainan, and  
177 Hong Kong launched two extra soundings per day, while three and two sounding  
178 stations in eastern and southeast Guangxi launched one extra sounding per day (at  
179 0600 UTC), with another extra sounding per day (at 1800 UTC) only for 10 days of  
180 each IOP. Moreover, a research flight was conducted by the Government Flying  
181 Service (GFS) of Hong Kong during the morning (around 2300 UTC – 0200 UTC) on  
182 16 June 2014 after its overhaul maintenance. It has been planned to collect  
183 observations over the Hong Kong Flight Information Region (green lines in Fig. 2a)  
184 using a new aircraft with both the dropsonde measurement system and in-situ data  
185 probe during the extended period of experiments in 2017-2018.

186 In order to obtain information about microphysical properties and kinematic

187 structure of the rainstorms, the field campaigns deployed a number of portable  
188 instruments including two C-band polarimetric (C-POL) radars, one C-band  
189 frequency-modulated continuous-wave (C-FMCW) radar, two 8-mm-wavelength  
190 cloud radars (MMCR), one micro rain radar (MRR), several raindrop disdrometers,  
191 and one microwave radiometer (Fig. 2b; Table 1). These instruments mostly  
192 participated in the field experiments in both 2013 and 2014, although the locations of  
193 some instruments slightly changed between the two years. To facilitate the wind  
194 retrieval using dual-Doppler measurements, a C-POL radar was placed about 48.5 km  
195 to the southwest of the Guangzhou operational weather radar in the 2013 and 2014  
196 IOPs (i.e., the Heshan C-POL radar in Fig. 2b), while another C-POL radar was  
197 placed 52.5 km northeast and 27.0 km northwest of the Yangjiang operational S-band  
198 radar in the 2013 and 2014 IOPs (labeled as A2 and B2 in Fig. 2b), respectively. The  
199 MMCR and MRR were placed at Sanshui (labeled as A1 in Fig. 2b) and Yangjiang  
200 (with the C-FMCW radar) (labeled as B1 in Fig. 2b) during the 2013 and 2014 IOPs,  
201 respectively. Specification of the MMCR, C-FMCW and C-POL radars can be found  
202 in Liu et al. (2015) (see Table 2 therein). Moreover, one S-band polarimetric (S-POL)  
203 radar started its normal operation at Zhuhai in early 2014 and its observational data  
204 during the 2014-2015 IOPs were archived in the SCMREX database. The raindrop  
205 disdrometers were placed around the Yangjiang area in the 2013/2014 IOPs and the  
206 Zhuhai area in the 2015 IOP, respectively, to complement the polarimetric radars and  
207 facilitate estimation of raindrop size distribution. The other portable instruments (e.g.,  
208 the C-POL radars, MMCR, C-FMCW radar) did not participate in the 2015 IOP. More

209 facilities will be used during the SCMREX 2016-2018 field campaigns, including a  
210 two-dimensional video disdrometer (2DVD) (Schönhuber et al. 2007) and one more  
211 C-POL radar.

### 212 **3. Overview of heavy rainfall events during the SCMREX-2014 IOP**

213 Figure 3 shows the time series of the number of rain gauges in Guangdong  
214 province within the enhanced observing area ( $110^{\circ}$ - $117^{\circ}$ E,  $20^{\circ}$ - $25^{\circ}$ N) that recorded  
215 extreme daily rainfall ( $>100$  or  $200$  mm  $\text{day}^{-1}$ ) and hourly rainfall ( $>20$  mm  $\text{h}^{-1}$ ),  
216 respectively, during the IOPs of 2013-2015. It can be observed that a number of heavy  
217 rainfall events occurred during each IOP. For brevity of discussion, however, only the  
218 major heavy rainfall events during the 2014 IOP are described hereinafter. The most  
219 intense precipitation events during the 2014 IOP occurred on 8, 11, 22, and 23 May  
220 (Fig. 4) with daily rainfall of more than 100 mm recorded by 89, 155, 34, 98 stations  
221 respectively. On 11 and 23 May, the daily rainfall even exceeded 200 mm at 45 and  
222 35 stations, respectively. Location of the most abundant rainfall varied notably among  
223 the days from the coastal regions as shown on 11 May (Fig. 4a) to the northern inland  
224 area such as 23 May (Fig. 4d).

#### 225 *3.1 Rainfall distribution and MCSs' evolution*

226 On 8 May 2014, daily heavy rainfall exceeding  $50$  mm  $\text{day}^{-1}$  exhibits a  
227 west-east-oriented band extending from southeast Guangxi to the Pearl River Delta  
228 area in Guangdong, with the heaviest daily rainfall of 100-200 mm located in the east  
229 of the rainband (Fig. 4a). Numerous convective clusters were observed around  
230 southwest Guangdong, southeast Guangxi, and the adjacent ocean to the east of

231 Zhanjiang (labeled as X in Fig. 5a-b) during late morning to early afternoon hours on  
232 8 May (Fig. 5a). Although few convective clusters developed over the coastal waters,  
233 some developed over the land and grew in length, leading to the formation of a  
234 quasi-linear MCS over Guangdong coastal area in the late afternoon (Fig. 5b). This  
235 linear MCS lasted for 10 hours, from 1600 Beijing Standard Time (BST; BST = UTC  
236 + 8h; BST is earlier than the local solar time of Guangdong province by  
237 approximately 11-41 minutes) on 8 May to 0200 BST on 9 May. The whole  
238 precipitation process contributed to about 90% of the daily rainfall amount over the  
239 Pearl River Delta area and its west on 8 May 2014.

240 On 11 May, extreme rainfall affected the central coastal area of Guangdong, with  
241 more than 200 mm day<sup>-1</sup> located mostly in the coastal region of the Pearl River Delta  
242 region, while heavy precipitation of 100-200 mm day<sup>-1</sup> fell over northern Guangxi  
243 (Fig. 4b). The extreme rainfall along the Guangdong coast on 11 May 2014 was  
244 generated mostly by two linearly shaped MCSs (labeled as 'A1' and 'A2' in Figs.  
245 5c-d) that sequentially moved along the coastline from Yangjiang to Shenzhen  
246 (labeled as X in Figs. 5c-d). The two MCSs had similar organizational characteristics,  
247 i.e., consisting of northeastward "echo training" convective cells (Doswell et al. 1996).  
248 During their development, new convective cells were continuously initiated at the  
249 southwestern periphery of the MCSs, leading to the growth and sustained  
250 development of MCSs. Another linear MCS (labeled as 'A3' in Figs. 5c-d) originated  
251 in Guangxi and then merged with the locally developed MCS A2 in the late afternoon  
252 (about 1700 BST).

253 On 22 May, widespread precipitation was distributed over Guangdong province  
254 except for its southwest portion (Fig. 4c). However, heavy rainfall of more than 100  
255 mm per day was confined over the northern mountains showing a narrow and nearly  
256 west-east-oriented rainband, along which five rain gauges recorded more than 200  
257 mm of daily precipitation (Fig. 4c). The extreme precipitation was produced  
258 sequentially by two MCSs (labeled as ‘B1’ and ‘B2’ in Figs. 5e-f). The first MCS (B1)  
259 was initiated around midnight at the windward slope in northern Guangdong, and it  
260 was rather slow-moving with a duration of about 9 hours (0200-1300 BST). The other  
261 MCS (B2) was a squall line that was initiated over northern Guangxi in the late  
262 afternoon of the previous day, moved southeastward into Guangdong at about 1100  
263 BST 22 May, and passed across Guangdong in about 11 hours. The quasi-stationary  
264 MCS B1 and the fast moving squall line MCS B2, respectively, contributed about 60%  
265 and 40% of the total precipitation to this extreme rainfall event in northern  
266 Guangdong.

267 On 23 May, daily precipitation exceeding 50 mm day<sup>-1</sup> showed a broad band  
268 extending from northern Guangdong southeastward to the coastal region from Hong  
269 Kong to Shanwei (labeled as circles in Fig. 4d), with the precipitation of more than  
270 200 mm day<sup>-1</sup> located mostly over central Guangdong and its coasts (Fig. 4d). The  
271 extreme-rain-producing MCS consisted of numerous well-defined,  
272 southwest-northeast-oriented band-shaped convective precipitation regions with  
273 reflectivity >35 dBZ (simply referred to herein as rainbands) during its life span (Figs.  
274 5g-h), exhibiting “band training” of the rainbands along the MCS (Luo et al. 2014).

275 The rainbands, with a length of about 50 km, appeared quasi-stationary and moved  
276 little, continuously generating rain over the same areas for nearly 20 hours (i.e.,  
277 0030-2030 BST). The rainband-training organization of extreme-rain-producing MCS  
278 has recently been noticed in central East China during the Meiyu season (Luo et al.  
279 2014), the western Guangdong coastal area on 10 May 2013 (Wang et al. 2014), and  
280 the eastern Guangdong coastal area on 20 May 2015 (Wu and Luo 2016).

### 281 *3.2 Environmental conditions*

282 Figure 6 shows synoptic background in which the heavy precipitation occurred  
283 over South China on 8, 11, 22, 23 May 2014. Of significance is that South China was  
284 dominated by southwesterly flows with relatively high equivalent potential  
285 temperature ( $\theta_e$ ) air in the lower-troposphere, i.e., the heavy precipitation took place  
286 in the warm sector. There was a northeast-southwest oriented shear line on 11 and 22  
287 May (Figs. 6b-c), respectively, which was at least 200-300 km away from the heavy  
288 rainfall region of interest. Near the southwest edge of the shear line was the  
289 linear-shaped MCS on 11 May (A3 in Figs. 5c-d) and 22 May (B2 in Figs. 5e-f)  
290 initiated in Guangxi.

291 The environmental conditions of the precipitation systems on the rainy days were  
292 characterized by moderate (about  $500\text{-}800\text{ J kg}^{-1}$  on 8 May) to large (about  $2400\text{-}3000$   
293  $\text{J kg}^{-1}$  on 22 May) convective available potential energy (CAPE), very small  
294 convective inhibition (CIN; mostly about  $10\text{ J kg}^{-1}$  or less), and high moisture content  
295 (precipitable water of about  $50\text{-}64\text{ mm}$ ) (e.g., Fig. 7). High correlations between LLJs  
296 and heavy rainfall events have been noticed in the United States (Maddox et al. 1979;

297 Schumacher and Johnson 2008) and northern Taiwan (Chen and Yu 1988). A signature  
298 of southwesterly low-level jets (LLJs) was more evident on 11 and 22 May relative to  
299 8 and 23 May 2014 (cf. Figs. 6b,c and Figs. 6a,d). Collective analysis of the data from  
300 the dense mesonets, wind profilers, and radars suggests that LLJ in the PBL,  
301 topography in northern Guangdong, and a cold pool left behind by previous-day  
302 convection appear to play an important role in the convective triggering and  
303 maintenance for the case on 23 May 2014 (Chen and Luo 2016). However,  
304 relationships between the conditions of low-level wind fields and the location of  
305 convective initiation that led to formation of the heavy-rain-producing MCSs in South  
306 China during the pre-summer rainy season deserve further investigation.

### 307 *3.3 Polarimetric radar measurements*

308 For the MCS over southwest Guangdong in the late afternoon of 8 May 2014  
309 (Fig. 8a; Fig. 5b) and the quasi-linear MCS over central Guangdong on the 22 May  
310 afternoon (Fig. 8b; B2 in Fig. 5f), range height indicator (RHI) scans were taken using  
311 the Heshan C-POL radar. The corresponding C-POL polarimetric measurements of  
312 the vertical cross sections (dashed lines in Fig. 8) are given in Fig. 9 showing the  
313 microphysical characteristics associated with the two MCSs. The RHI scan on 8 May  
314 went through a convective precipitation region (at about 43-55 km in Figs. 9a-d)  
315 embedded within wider stratiform precipitation areas. The convective precipitation  
316 within the MCS was characterized by strong  $Z_H$  (~50-55 dBZ) associated with a  
317 column of high values of differential reflectivity ( $Z_{DR} > 1.0$  dB) and specific  
318 differential phase shift ( $K_{DP} > 4.0$  ° km<sup>-1</sup>) at about 45-48 km in Figs. 9a,b,c. As  $Z_{DR}$

319 provides information about the oblateness of particles and  $K_{DP}$  depends on liquid  
320 water content (Bringi and Chandrasekar 2001), the positive  $Z_{DR}$  and  $K_{DP}$  column  
321 suggest rain drops extending up to 5.5-km altitude, about 0.9 km above the  $0^{\circ}\text{C}$  level  
322 (4.6 km according to sounding data). At 50-54 km in Figs. 9a-c, the values of  $Z_H$ ,  $Z_{DR}$ ,  
323 and  $K_{DP}$  increase from  $0^{\circ}\text{C}$  level downward suggesting a signature of warm rain. The  
324 stratiform precipitation regions were characterized by a brightband signature of low  
325 values of zero-lag cross-correlation coefficient ( $\rho_{HV}$ , 0.92 to 0.95) and high values of  
326  $Z_H$  (about 35-40 dBZ) and  $Z_{DR}$  (about 1.0 dB) at  $0^{\circ}\text{C}$  level. On the other hand, the  
327 RHI scan on 22 May (Figs. 9e-h) mainly detected convective precipitation regions  
328 and the adjacent anvil clouds. The stronger and deeper convection on 22 May had  
329 large  $Z_H$  (about 50-55 dBZ) extending up to 7 km at about 33-35 km in Fig. 9e, well  
330 above the  $0^{\circ}\text{C}$  level (5.2 km according to sounding data). The lower  $\rho_{HV}$  (0.94-0.96)  
331 from  $0^{\circ}\text{C}$  level to 7 km in the deep convective region (at about 33-35 km in Fig. 9h)  
332 suggest mixtures of ice (hail or irregular snow) and raindrops. In the meantime, the  
333 high values of  $K_{DP}$  ( $3.0\text{-}3.5 \text{ }^{\circ} \text{ km}^{-1}$ ) and  $Z_{DR}$  (1.25-1.75 dB) in the lower-topped  
334 convection (at about 27-30 km in Fig. 9e) were located at 2-4 km altitudes. Below 2  
335 km altitude, the  $K_{DP}$  and  $Z_{DR}$  decreasing toward the ground suggest breakup of large  
336 raindrop by the updraft.

#### 337 **4. Preliminary Research Highlights**

##### 338 *4.1 Impact of assimilating WPR data on convection-permitting QPF*

339 Vertical profiles of horizontal winds measured by fourteen WPRs over  
340 Guangdong were assimilated into a partial-cycle data assimilation system, based on

341 the three-dimensional variational method, using the Global/Regional Assimilation and  
342 PrEdiction System (GRAPES) (Zhang and Shen 2008; Chen et al. 2008; Xue et al.  
343 2008) with horizontal resolution of  $0.03^\circ \times 0.03^\circ$  in regular latitude-longitude  
344 coordinates. The impact of assimilating the WPR data on the 0–12-h QPF in South  
345 China during May 2014 was evaluated by comparing the forecasts from two monthly  
346 continuous experiments: one with the WPR data assimilated (WPR\_DA) and the other  
347 without it (no\_WPR\_DA). In each of the two experiments, analysis-forecast cycles  
348 over a 30-day period in May 2014 were performed.

349 The comparison results indicate that assimilating the quality-controlled WPR  
350 data significantly improves the 0-6h forecasts of the vertical structures of  
351 meteorological variables (e.g., U-wind shown in Fig. 10a) and the diagnostic fields at  
352 the surface (e.g., the surface wind field in Fig. 10b). For example, the  
353 root-mean-square error (RMSE) of U-wind at 200 hPa decreased from  $5.71 \text{ m s}^{-1}$  to  
354  $5.31 \text{ m s}^{-1}$ ; the RMSE of the 10-m wind speed decreased from  $3.48 \text{ m s}^{-1}$  to  $3.13 \text{ m s}^{-1}$   
355 for the 3-h lead time. WPR\_DA also improves the QPF skill throughout the 12-h  
356 forecast period by reducing the predicted spurious precipitation and alleviating  
357 overestimations and false alarms. The biases in the heavy rainfall ( $>20 \text{ mm h}^{-1}$ )  
358 forecast were reduced by about 30% (Fig. 10c). Moreover, assimilating the WPR data  
359 improves the fractions skill score (FSS) (Roberts 2008; Mittermaier and Roberts 2010)  
360 by 12% for the heavy rainfall ( $>20 \text{ mm h}^{-1}$ ) prediction at mesoscale (about 200 km)  
361 (Fig. 10d) and by 31% for the extremely rainfall ( $>40 \text{ mm h}^{-1}$ ) prediction at smaller  
362 scales (about 25 km) (not shown). Further case studies suggest that the improved

363 representations of wind and moisture at the lower levels after assimilating the WPR  
364 data lead to more reasonable descriptions of convective development and the  
365 associated rainfall production (Zhang et al. 2016).

#### 366 *4.2 Improving a cloud microphysical parameterization scheme*

367 The squall line that occurred on 22 May 2014 was explicitly simulated in  
368 nonhydrostatic and convection-permitting configuration, with a two-way triply nested  
369 domain (grid spacing of 27/9/3 km), using the Advanced Research core of the  
370 Weather Research and Forecasting (ARW-WRF, Skamarock et al. 2008) model.  
371 Several microphysical schemes, including the SBU-YLIN scheme (Lin and Colle  
372 2011) and Morrison scheme (Morrison et al. 2005), were applied for comparing the  
373 simulations of the squall line. All the domains were initialized at 1200 UTC (or 2000  
374 BST) 21 May 2014 and integrated for 24 hours. The NCEP FNL reanalysis with 6-h  
375 interval was used for the model initial and outermost lateral boundary conditions.

376 Surface cooling rates, an indication of the cold pool strength, were as strong as  
377 -3 K in the observations at 0800 UTC (Fig. 11d). However, they are nearly zero in the  
378 simulation with the original SBU-YLIN scheme (Fig. 11a). This disagreement largely  
379 explains why the squall line was missed in this simulation as the presence of a cold  
380 pool is critical for the maintenance and movement of a squall line (Rotunno et al.  
381 1988). Through a series of sensitivity tests and detailed investigations, the failure of  
382 the original SBU-YLIN scheme to capture the evolution of the squall line is traced  
383 down to two major factors: turnoff of rain evaporation in environment with relative  
384 humidity greater than 90%, and the saturation adjustment method of Tao et al. (1989).

385 Rain evaporation tendency in the scheme is computed based on the conditions at the  
386 beginning of each time step, but applied over the whole length of the time step. This  
387 might lead to supersaturation during this time step due to evaporative cooling, which  
388 makes rain evaporation non-physical, especially for large time steps. In the original  
389 SBU-YLIN scheme, the solution for partially preventing this was to disallow rain  
390 evaporation to increase RH above 90% within the grid cell at the end of the time step  
391 based on the initial saturation mixing ratio. As a result, rain evaporation is inhibited  
392 below the cloud base since RH is greater than 90% most of the time during the  
393 simulation. This is undesirable and we adopted a new method proposed by Peter N.  
394 Blossey (personal communication), in which the amount of rain evaporation that  
395 would produce saturation (accounting for the change in saturation mixing ratio due to  
396 evaporative cooling) is calculated and the evaporation is kept smaller than 0.9 of this  
397 amount in magnitude. The modification enables the rain evaporation even in  
398 relatively moist environment, which favors the initiation of cold pool and the  
399 maintenance of the squall line. In the saturation adjustment method of Tao et al.  
400 (1989), saturation vapor pressure was calculated by the grid box temperature without  
401 considering the cooling associated with cloud evaporation and ice sublimation, i.e.,  
402 only suitable for cloud-free situation. This can lead to frequent fluctuations between  
403 cloud-free and cloudy situations in a grid box. To alleviate this problem, the  
404 calculation of saturation vapor pressure was refined by including the cooling effect  
405 associated with cloud evaporation and ice sublimation, and thus became more suitable  
406 for both cloud-free and cloudy situations. This fix further improved the simulation of

407 the squall line, including its movement and morphology.

408         With these two modifications, the simulation is significantly improved in the  
409 strength of the cold pool, movement of the squall line, the total precipitation produced,  
410 and the trailing stratiform precipitation (Fig. 11b). These results suggest that the  
411 weakness of the original SBU-YLIN scheme in simulating squall lines is not solely  
412 due to the small terminal velocity of precipitating ice as recently pointed out by  
413 Morrison et al. (2015). This example also highlights the importance of SCMREX for  
414 providing cases for model physics evaluation and improvement. More detailed  
415 analyses about the sensitivity to various cloud microphysical parameterization  
416 schemes, modifications to the original SBU-YLIN scheme and the resultant impacts  
417 on the simulations, as well as comparisons between a double moment version of the  
418 SBU-YLIN scheme and its original single moment version will be published in the  
419 future.

## 420 **5. Summary and Future Research**

421         An extensive array of meteorological instrumentation was deployed during the  
422 SCMREX pilot field campaigns of 2013-15 to investigate the characteristics of  
423 mesoscale weather systems producing extreme rainfall over South China during the  
424 pre-summer rainy season. Extreme daily rainfall was produced by long-lived MCSs  
425 with a linear alignment of convective cells that favored persistent and large rainfall  
426 accumulation over the same region. The characteristics of the extreme-rain-producing  
427 MCSs during SCMREX that led to heavy rainfall (their duration, organizational  
428 patterns, and quasi-stationary behavior) appear to be attributable to the characteristic

429 environmental conditions during the pre-summer rainy season. Namely, these systems  
430 occurred in prevailing southwesterly monsoonal flows providing sufficient moisture  
431 even without the presence of an LLJ over complex underlying surfaces in South  
432 China (e.g., land/sea contrast, and mountains near the coasts and inland facilitating  
433 continuous convective initiation), and within a series of feedbacks from MCSs (i.e.,  
434 convectively generated cold outflow boundaries where continuous convective  
435 initiation usually takes place), as discussed by Wang et al. (2014) and Wu and Luo  
436 (2016).

437 Further in-depth observational and modeling studies are necessary to achieve the  
438 scientific objectives of SCMREX. In particular, our ability to predict the timing and  
439 location of convective initiation is very limited, due partly to the lack of sufficient  
440 high-resolution observations and partly to the insufficient understanding of the impact  
441 of terrain, land surface inhomogeneity, and convectively generated surface boundaries.  
442 For example, convective initiation appeared to be more favorable over the west  
443 Guangdong coast on 10 May 2013 (Wang et al. 2014) and west to central Guangdong  
444 coast 11 May 2014 (Figs. 5c-d), over the northern mountainous regions of Guangdong  
445 on 22 May 2014 (Fig. 5e), and over both northern Guangdong and eastern Guangdong  
446 coast on 23 May 2014 (Figs. 5g-h). Organizational modes and movement  
447 characteristics of MCSs also varied among the days and even on the same days (Fig.  
448 5). More comprehensive studies are needed to reveal the underlying physical  
449 mechanisms to account for such differences. Moreover, measurements from the  
450 polarimetric radars, MRRs, MMCR, C-FMCW radar, and disdrometers will be

451 analyzed more carefully in order to quantitatively unravel the characteristics of cloud  
452 and precipitation processes over South China during the pre-summer rainy season and  
453 compare with those over other regions, e.g., southern Taiwan during the Southwest  
454 Monsoon Experiment/Terrain-Influenced Monsoon Rainfall Experiment  
455 (SoWMEX/TiMREX; Jou et al. 2011). Results of numerical experiments using  
456 convection-permitting NWP models will be post-processed using simulators such as  
457 the polarimetric radar data simulator (Jung et al. 2008) to make “apple-to-apple”  
458 comparisons with the observations. Such comparisons will facilitate further research  
459 development to improve the parameterizations of cloud-precipitation microphysics  
460 such as the SBU-YLIN scheme and a newly developed scheme based on observations  
461 over East China (Yin 2013). Furthermore, the impact study of assimilating WPR data  
462 on QPF (Zhang et al. 2016) will be extended to the operational weather radars and the  
463 polarimetric radars. Effects of land surface processes in the variability of ensemble  
464 simulations will also need to be investigated, such as by using different combinations  
465 of sub-processes and parameters in Noah-MP LSM of WRF (Niu et al. 2011).

466

#### 467 **Acknowledgements**

468 This work was jointly funded by the Public Welfare Scientific Research Projects in  
469 Meteorology (GYHY201406013, GYHY201406003, GYHY201306004), Scientific  
470 Research Projects of the Chinese Academy of Meteorological Sciences (CAMS)  
471 (2014Z004), Outreach Projects of the State Key Laboratory of Severe Weather  
472 (2014LASW-B04, 2014LASW-B05), and the National Basic Research Program of

473 China (973 Program; 2012CB417202, 2014CB441402). We would like to  
474 acknowledge the Hong Kong Observatory for their additional sounding observations  
475 and the data collection flight; the Guangdong Meteorological Bureau for providing  
476 the WPR data, the additional sounding observations, and logistical support; and the  
477 Center of Data Analysis and Application of CAMS for archiving SCMREX data. We  
478 would also like to thank the Guangxi Meteorological Bureau and the Hainan  
479 Meteorological Bureau for their additional sounding observations.

480

481

### References

482 Bringi, V. N., and V. Chandrasekar, 2001: *Polarimetric Doppler Weather*  
483 *Radar-Principles and Applications*. Cambridge University Press, 636 pp.

484 Chen, Y., and Y. Luo, 2016: Mesoscale observational analysis of an extreme rainfall  
485 event during the SCMREX-2014. Paper presented at *Chinese-American Oceanic*  
486 *and Atmospheric Association (COAA) 2016 Conference*, Beijing, July 27-30,  
487 2016.

488 Chen, D. H., J. S. Xue, X. S. Yang, and co-authors, 2008: New generation of  
489 multiscale NWP system (GRAPES): General scientific design. *Chinese Science*  
490 *Bulletin*, **53**, 3433–3445.

491 Chen, G. T.-J., and C.-C. Yu, 1988: Study of low-level jet and extremely heavy  
492 rainfall over northern Taiwan in the Mei-yu season. *Mon. Wea. Rev.*, **116**,  
493 884-891.

494 Cummins, K. L., M. J. Murphy, E. A. Bardo, and Co-authors, 1998: A combined  
495 TOA/MDF technology upgrade of the U.S. National Lightning Detection  
496 Network. *J. Geophys. Res. Atmos.*, **103**(D8): 9035-9044.

497 Ding, Y.H., 1994: Monsoons over China. Kluwer Academic Publishers, The  
498 Netherlands. 419 pp.

499 Doswell, C. A., III, H. E. Brooks, and R. A. Maddox, 1996: Flashflood forecasting:  
500 An ingredients-based methodology, *Wea. Forecasting*, **11**, 560–581.

501 Huang, S. S., 1986: Heavy rainfall over Southern China in the pre-summer rainy  
502 season. Guangdong Science and Technology Press, 244 pp. (in Chinese)

503 Jou, B. J.-D., W.-C. Lee, and R. H. Johnson, 2011: An overview of  
504 SoWMEX/TiMREX and its operation. *The Global Monsoon System: Research  
505 and Forecast*, 2<sup>nd</sup> ed., C.-P. Chang, Ed., World Scientific, 303-318.

506 Jung, Y., G. Zhang, and M. Xue, 2008: Assimilation of simulated polarimetric radar  
507 data for a convective storm using the ensemble Kalman filter. Part I: Observation  
508 operators for reflectivity and polarimetric variables. *Mon. Wea. Rev.*, **136**(6),  
509 2228-2245.

510 Lin, Y., and B. A. Colle, 2011: A new bulk microphysical scheme that includes  
511 riming intensity and temperature-dependent ice characteristics. *Mon. Wea. Rev.*,  
512 **139**, 1013–1035.

513 Liu, L., J. Zheng, Z. Ruan, and co-authors, 2015: Comprehensive radar observations  
514 of clouds and precipitation over the Tibetan Plateau and preliminary analysis of

515 cloud properties. *J. Meteor. Res.*, **29**(4), 546–561, doi:  
516 10.1007/s13351-015-4208-6.

517 Luo, Y. L., 2016: Advances in understanding the early-summer heavy rainfall over  
518 South China. Invited review chapter in *The Global Monsoon System, III*, a  
519 WMO Quadrennial Review. Editors: C.P. Chang, N. G. Lau, R. H. Johnson, B.  
520 Wang and M. Wheeler. Vol. 9, World Scientific Series on Asia-Pacific Weather  
521 and Climate, in press.

522 Luo, Y., Y. Gong, and D.-L. Zhang, 2014: Initiation and organizational modes of an  
523 extreme-rain-producing mesoscale convective system along a Mei-Yu front in  
524 East China. *Mon. Wea. Rev.*, **142**, 203–221.

525 Luo, Y., H. Wang, R. Zhang, and co-authors, 2013: Comparison of rainfall  
526 characteristics and convective properties of monsoon precipitation systems over  
527 South China and the Yangtze and Huai river basin. *J. Climate*, **26**, 110–132.

528 Maddox, R. A., C. F. Chappell, and L. R. Hoxit, 1979: Synoptic and meso- $\alpha$  scale  
529 aspects of flash flood events. *Bull. Amer. Meteor. Soc.*, **60**, 115–123.

530 Morrison, H., J. A. Curry, and V. I. Khvorostyanov, 2005: A new double moment  
531 microphysics parameterization for application in cloud and climate models. Part  
532 I: Description. *J. Atmos. Sci.*, **62**, 1665–1677.

533 Morrison H., J. A. Milbrandt, G. H. Bryan, and co-authors, 2015: Parameterization of  
534 cloud microphysics based on the prediction of bulk ice particle properties. Part II:  
535 Case study comparisons with observations and other schemes. *J. Atmos. Sci.*, **72**,  
536 312–339.

537 Mittermaier, M., and N. Roberts, 2010: Intercomparison of spatial forecast  
538 verification methods: Identifying skillful spatial scales using the fractions skill  
539 score. *Wea. Forecasting*, **25**, 343–354.

540 Niu, G-Y, Z.-L. Yang, K. E. Mitchell, and co-authors, 2011: The community Noah  
541 land surface model with multiparameterization options (Noah-MP): 1. Model  
542 description and evaluation with local-scale measurements. *J. Geophys. Res.*, **116**,  
543 D12109. doi:10.1029/2010JD015139

544 Roberts, N. M., 2008: Assessing the spatial and temporal variation in the skill of  
545 precipitation forecasts from an NWP model. *Meteor. Appl.*, **15**, 163–169.

546 Rotunno, R., J. B. Klemp, and M. L. Weisman, 1988: A theory for strong, long-lived  
547 squall lines. *J. Atmos. Sci.*, **45** (3), 463-485.

548 Schönhuber, M., G. Lammer, and W. Randeu, 2007: One decade of imaging  
549 precipitation measurement by 2D-video-distrometer. *Adv. Geosci.*, **10**(10),  
550 85-90.

551 Schumacher, R.S., and R.H. Johnson, 2008: Mesoscale processes contributing to  
552 extreme rainfall in a midlatitude warm-season flash flood. *Mon. Wea. Rev.*, **136**,  
553 3964-3986.

554 Skamarock, W. C., and Coauthors, 2008: A description of the Advanced Research  
555 WRF version 3. NCAR Tech. Note NCAR/TN-4751STR, 113 pp. [Available  
556 online at [http://www.mmm.ucar.edu/wrf/users/docs/arw\\_v3.pdf](http://www.mmm.ucar.edu/wrf/users/docs/arw_v3.pdf).]

557 Tao, W.-K., J. Simpson, and M. McCumber, 1989: An ice-water saturation  
558 adjustment. *Mon. Wea. Rev.*, **117**, 231–235.

559 Wang, H., Y. L. Luo, B. Jou, 2014: Initiation, maintenance, and properties of  
560 convection in an extreme rainfall event during SCMREX. *J. Geophys. Res.*  
561 *Atmos.*, **119**, 13,206–13,232, doi:10.1002/2014JD022339.

562 Wu, M., and Y. Luo, 2016: Mesoscale observational analysis of lifting mechanism of  
563 a warm-sector convective system producing the maximal daily precipitation in  
564 China mainland during pre-summer rainy season of 2015. *J. Meteor. Res.*, **30**(5),  
565 doi:10.1007/s13351-016-6089-8. (in press)

566 Xia, R., D.-L. Zhang and B. Wang, 2015: A 6-yr cloud-to-ground lightning  
567 climatology and its relationship to rainfall over central and eastern china. *J.*  
568 *Applied Meteor. Climatology*, **54**, 2443-2460.

569 Xue, J. S., S. Y. Zhuang, G. F. Zhu, and co-authors, 2008: Scientific design and  
570 preliminary results of three-dimensional variational data assimilation system of  
571 GRAPES. *Chinese Science Bulletin*, **53**, 3446–3457.

572 Yin, J., 2013. The study on observation and parameterization of cloud-precipitation  
573 microphysical properties over East Asia. Doctoral thesis, Zhejiang University,  
574 Hangzhou, China, 163pp. (In Chinese)

575 Zhang, Y. J., W. T. Lu, D. Zheng, and co-authors, 2014: Evaluation for the  
576 performance of the Guangdong-Hongkong-Macau Lightning Location System.  
577 Paper presented at *the 23th International Lightning Detection Conference*,  
578 Tucson, Arizona, USA.

579 Zhang, X. B., Y. L. Luo, Q. L. Wan, and co-authors, 2016: Impact of assimilating  
580 wind profiling radar observations on convection-permitting quantitative  
581 precipitation forecasts during SCMREX. *Wea. Forecasting*, **31**, 1271-1292.

582 Zhang, R.H., Y.Q. Ni, L.P. Liu, and co-authors, 2011: South China Heavy Rainfall  
583 Experiments (SChEREX). *J. Meteor. Soc. Japan*, **89A**, 153-166.

584 Zhang, R.H., and X.S. Shen, 2008: On the development of the GRAPES - A new  
585 generation of the national operational NWP system in China. *Chin. Sci. Bull.*, **53**,  
586 3429-3432.

587 Zhou, X.-J., 2003: Heavy Rainfall Experiment in South China during Pre-summer  
588 Rainy Season (HUAMEX), 1998. Beijing: China Meteorological Press, 220pp.  
589 (in Chinese)

590 Zhu, X., and J. Zhu, 2004: New generation weather radar network in China (in  
591 Chinese), *Meteor. Sci. Technol.*, **32**, 255–258.

592

593

594

**Table 1. Major instruments deployed during the SCMREX-2014 field campaign**

| <b>Instrument or station</b>                              | <b>Number</b>   | <b>Coverage or location</b>   |
|---|---|---|
| Automated weather station                                 | 1946  | 110°-117°E, 21-25°N   |
| Radiosonde station with additional launches               | 8<br>[3 in Guangdong, 1 in Hong Kong, 2 in southeast Guangxi, 2 in Hainan ] | See Fig. 2a   |
| Operational Doppler radar                                 | 14  | 110°-117°E, 21°-25°N  |
| Polarimetric Radar  | 3<br>[Zhuhai S-POL, Heshan C-POL, and Yangjiang C-POL radars]               | (113.370°E, 22.027°N),<br>(112.981°E, 22.737°N),<br>(111.788°E, 22.011°N) |
| Wind-profiling radar                                      | 17  | (110°-117°E, 21-25°N)<br>(See Fig. 2a)                                    |
| Disdrometer   | 7   | See Fig. 2b   |
| 8-mm-wavelength cloud radar (MMCR)                        | 2   | (111.979°E, 21.845°N),<br>(111.788°E, 22.011°N)                           |
| Micro rain radar  | 1   | (111.979°E, 21.845°N)   |
| C-band frequency modulated continuous wave (C-FMCW) radar | 1   | (111.979°E, 21.845°N)   |
| Microwave radiometer                                      | 1   | (111.979°E, 21.845°N)   |
| Lightning detector  | 17  | 14 are shown in Fig. 2b   |

595

596

598 Figure 1 (a) Distribution of the seasonal mean rainfall accumulated during April-June  
599 of 1981-2012 based on the national surface meteorological stations over South  
600 China. (b) Topography over South China (shadings), overlaid by 800 mm and  
601 1000 mm contours of the seasonal mean rainfall that are denoted by blue and red  
602 lines, respectively. Thin dashed lines denote the borders between provinces.  
603 Names of the six provinces and the three coastal cities (denoted by stars) are  
604 labeled. Thin solid lines highlight the enhanced observing area ( $110^{\circ}$ - $117^{\circ}$ E,  
605  $20^{\circ}$ - $25^{\circ}$ N).

606 Figure 2 Distribution of major observing facilities that participated during the  
607 SCMREX pilot field campaigns over (a) South China and its vicinity; and (b)  
608 central and western Guangdong Province where the portable instruments were  
609 placed during the 2013-2015 IOPs. In (a), orange and green lines highlight the  
610 enhanced observing area ( $110^{\circ}$ - $117^{\circ}$ E,  $20^{\circ}$ - $25^{\circ}$ N) and the aircraft observing area,  
611 respectively; and the circles with a radius of 150 km are centered at the  
612 operational S-band radars approximately representing their PPI scanning range.  
613 In panel (b), grey shadings represent topography, light blue line denote the  
614 boundary of the Pearl River Delta area, and A1 and A2 (B1 and B2) denote the  
615 places with most portable instruments in 2013 (2014) IOPs. All the facilities are  
616 consistent with markers in the legend.

617 Figure 3 Time series of the number of rain gauges in Guangdong province within the  
618 SCMREX enhanced observing area (orange rectangle lines in Fig. 2b) that  
619 recorded extremely daily rainfall ( $>200$  mm  $\text{day}^{-1}$ , red lines;  $>100$  mm  $\text{day}^{-1}$ ,  
620 blue lines) and heavy hourly rainfall ( $>20$  mm  $\text{h}^{-1}$ , grey bars) during (a) 2013, (b)  
621 2014, and (c) 2015 IOPs. The total number of rain gauges was 1269 within the  
622 analysis area.

623 Figure 4 Distribution of daily (0000 – 0000 BST) rainfall (mm) over the SCMREX  
624 enhanced observing area (orange rectangle lines in Fig. 2a) on (a)–(d) 8, 11, 22,  
625 and 23 May 2014. Gray shadings represent topography. The black circles in (c)  
626 denote the locations of the sounding stations at Qingyuan and Yangjiang, while  
627 the black crosses in (d) denote the locations of the operational S-band radars at  
628 Hong Kong and Shanwei.

629 Figure 5 Radar reflectivity at 3-km altitude ASL in the enhanced observing area  
630 (orange rectangle lines in Fig. 2a) derived from nine operational weather radars  
631 (8 in Guangdong and 1 in east Guangxi) at two selected times on (a, b) 08 May,  
632 (c, d) 11 May, (e, f) 22 May, and (g, h) 23 May 2014, respectively. Gray shadings  
633 represent topography. The black crosses denote the locations of the operational  
634 S-band radars at Zhanjiang, Yangjiang, and Shenzhen, respectively. Ellipses in (c,  
635 d) and (e, f) denote the individual MCSs on 11 May and 22 May, respectively.

636 Figure 6 The ERA-interim analysis of 850 hPa at 0800 BST (a) 8 May, (b) 11 May, (c)  
637 22 May, and (d) 23 May, 2014, showing the equivalent potential temperature ( $\theta_e$ ,  
638 contoured at intervals of 5 K, with the 345 K contour in red) superimposed with  
639 horizontal wind barbs, and also precipitable water (mm, shaded). A full barb is 5  
640  $\text{m s}^{-1}$ . Shear lines at 850 hPa are shown by thick purple lines. The 588 dgpm  
641 contours of the geopotential height at 500 hPa are denoted by blue dashed lines.  
642 Pink stars denote locations of the heavy rainfall of interest on the corresponding  
643 days.

644 Figure 7 (a)-(d) Skew T-log  $P$  diagram at Yangjiang sounding station (59663) at 02  
645 BST and 08 BST on (a, b) 8 May and (c,d) 11 May 2014. (e)-(h) As (a)-(d), but  
646 for Qingyuan sounding station (59280) on (e, f) 22 May and (g, h) 23 May 2014.  
647 The soundings on 8 May, at 02 BST of 11 May, and on 23 May were influenced  
648 by rain evaporative cooling near the surface and corrected based on the  
649 observations from the surface AWSs around the sounding station. The original  
650 soundings without the correction are shown in the panels as short dashed lines,  
651 while the corrected soundings are shown as solid lines. The values of CAPE,  
652 CIN, LCL, LFC, and LNB were calculated for the mass-weighted near surface  
653 air (0-500 m) after the correction.

654 Figure 8 CAPPI at 3 km ASL derived from the Guangzhou S-band radar volumetric  
655 scans at about (a) 1754 BST 8 May and (b) 1606 BST 22 May 2014. Cross and  
656 star denote locations of the Guangzhou radar and the Heshan C-POL radar,  
657 respectively. Black dashed lines represent the locations of the vertical cross  
658 sections to be shown in Fig. 9.

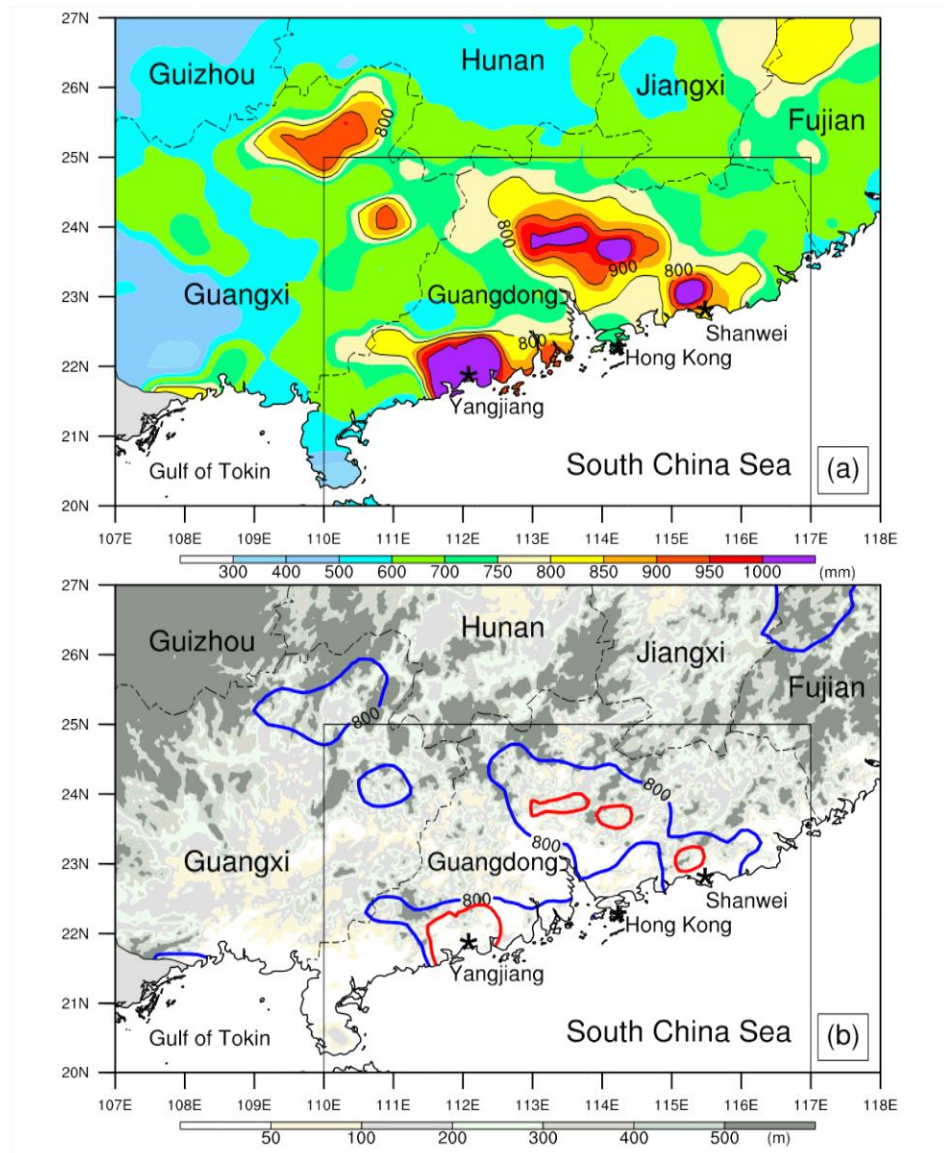
659 Figure 9 (a)-(d) Vertical cross section at about 1752 BST 8 May of the Heshan C-POL  
660 measurements of (a) reflectivity (dBZ), (b) differential reflectivity ( $Z_{dr}$ ), (c)  
661 specific differential phase ( $K_{dp}$ ), and (d) correlation coefficient ( $\rho_{hv}$ ). The black

662 dashed and solid lines represent the 0°C level (4.6 km) and -15°C level (7 km),  
663 respectively, according to sounding data. (e)-(h) As in (a)-(d), but at about 1604  
664 BST 22 May 2014 and the 0°C (-15°C) level is 5.2 km (8.1km).

665 Figure 10 (a) Vertical profiles of root mean square errors (RMSEs) of the 12-h  
666 forecasts of U-wind with respect to radiosonde observations in the two monthly  
667 continuous experiments with (WPR\_DA; solid lines) and without (no\_WPR\_DA;  
668 dotted lines), respectively, the WPR measurements being assimilated. (b) RMSEs  
669 for the forecasts of horizontal wind speed at 10 m altitude AGL with respect to  
670 surface observations in no\_WPR\_DA (light bars) and WPR\_DA (dark bars) as a  
671 function of lead time. (c) Bias for the forecasts of 1-h accumulated precipitation (>  
672 20 mm) averaged over different lead times in no\_WPR\_DA (gray bars) and  
673 WPR\_DA (dark bars). (d) Fractions skill score (FSS) for the forecasts of 1-h  
674 accumulated precipitation averaged over different lead times with precipitation  
675 threshold of 20 mm and neighborhood length of 200 km in no\_WPR\_DA (gray  
676 bars) and WPR\_DA (dark bars). Dark triangles indicate that the significance  
677 level of the difference of (a, b) RMSE, (c) bias, and (d) FSS between WPR\_DA  
678 and no\_WPR\_DA is greater than 90%.

679 Figure 11 Radar reflectivity (dBZ; color shaded) and wind barbs at 0.5 km ASL at  
680 0800 UTC 22 May 2014, the 0400-0800 UTC total precipitation (mm; magenta  
681 dashed lines), surface air temperature changes from 0700UTC to 0800UTC (K  
682 per hour; blue solid lines), hourly precipitation ending at 0800 UTC (mm; black  
683 dashed lines), and the location of the squall line during the previous 4 hours  
684 (cyan dashed lines with red number denoting the time) from simulations using (a)  
685 the default SBU-YLIN scheme, (b) the improved SBU-YLIN scheme, (c) the  
686 Morrison scheme (c), and (d) from the observations except for without the wind  
687 barbs. The area covered by the -3 K h<sup>-1</sup> contour of surface cooling rate is  
688 approximately an indication of the cold pool. The black dot in (d) depicts the  
689 location of the Guangzhou radar.

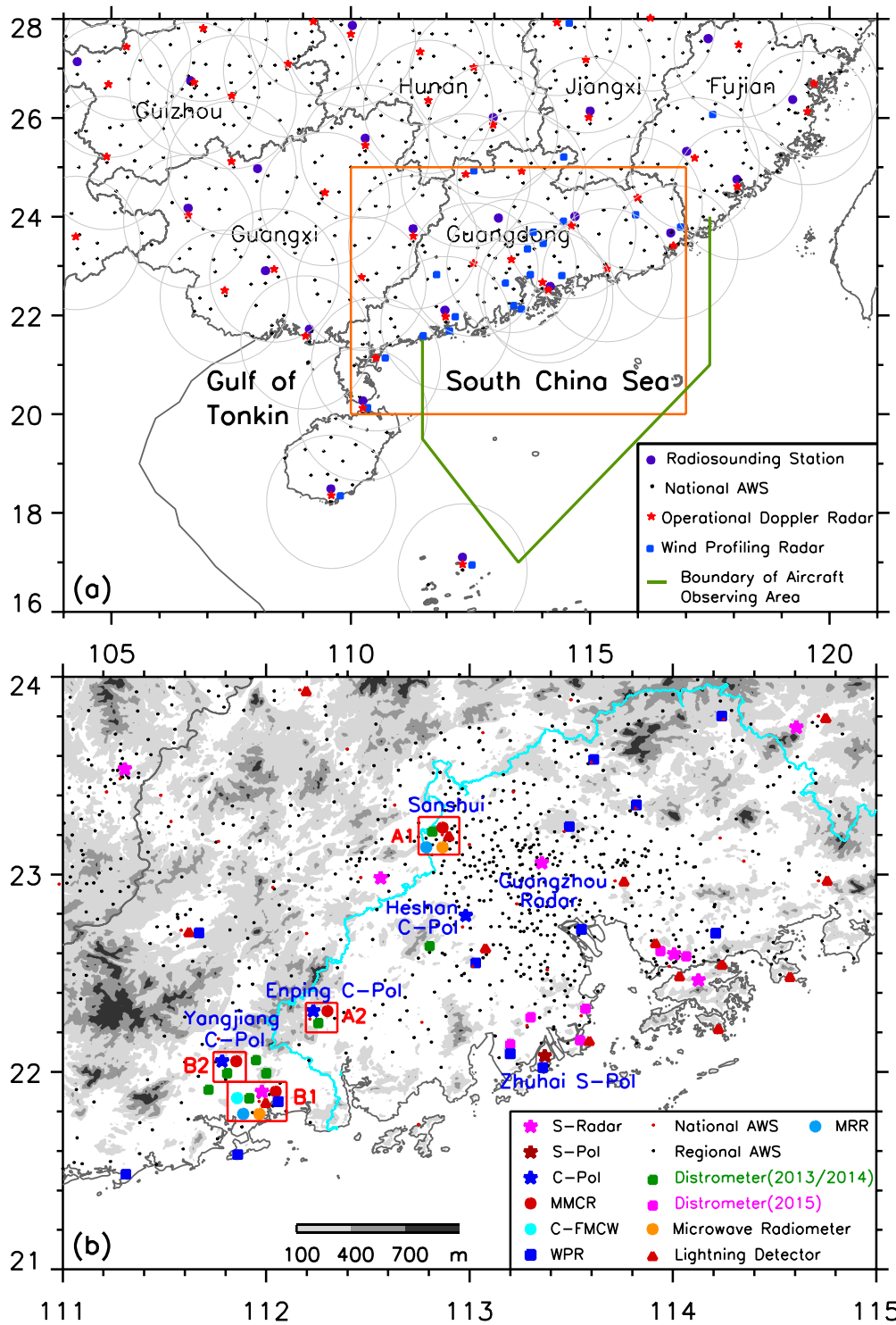
690  
691  
692



693

694 Figure 1 (a) Distribution of the seasonal mean rainfall accumulated during April-June  
 695 averaged of 1981-2012 based on the national surface meteorological stations  
 696 over South China. (b) Topography over South China (shadings), overlaid by 800  
 697 mm and 1000 mm contours of the seasonal mean rainfall that are denoted by  
 698 blue and red lines, respectively. Thin dashed lines denote the borders between  
 699 provinces. Names of the six provinces and the three coastal cities (denoted by  
 700 stars) are labeled. Thin solid lines highlight the enhanced observing area  
 701 (110°-117°E, 20°-25°N).

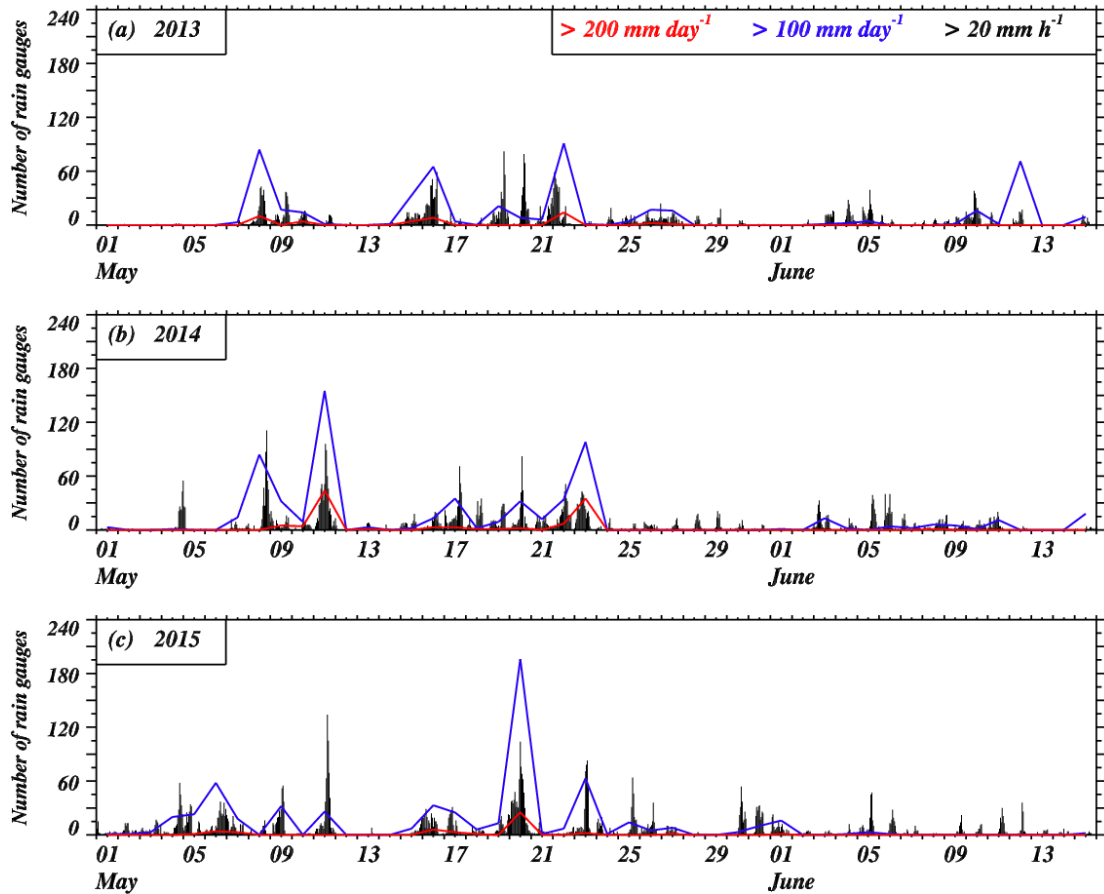
702



703

704 Figure 2 Distribution of major observing facilities that participated during the  
 705 SCMREX pilot field campaigns over (a) South China and its vicinity; and (b)  
 706 central and western Guangdong Province where the portable instruments were placed during  
 707 the 2013-2015 IOPs. In (a), orange and green lines highlight the enhanced observing  
 708 area ( $110^{\circ}$ - $117^{\circ}$ E,  $20^{\circ}$ - $25^{\circ}$ N) and the aircraft observing area, respectively; and the

709 circles with a radius of 150 km are centered at the operational S-band radars  
 710 approximately representing their PPI scanning range. In panel (b), grey shadings  
 711 represent topography, light blue line denote the boundary of the Pearl River Delta area,  
 712 and A1 and A2 (B1 and B2) denote the places with most portable instruments in 2013  
 713 (2014) IOPs. All the facilities are consistent with markers in the legend.  
 714  
 715

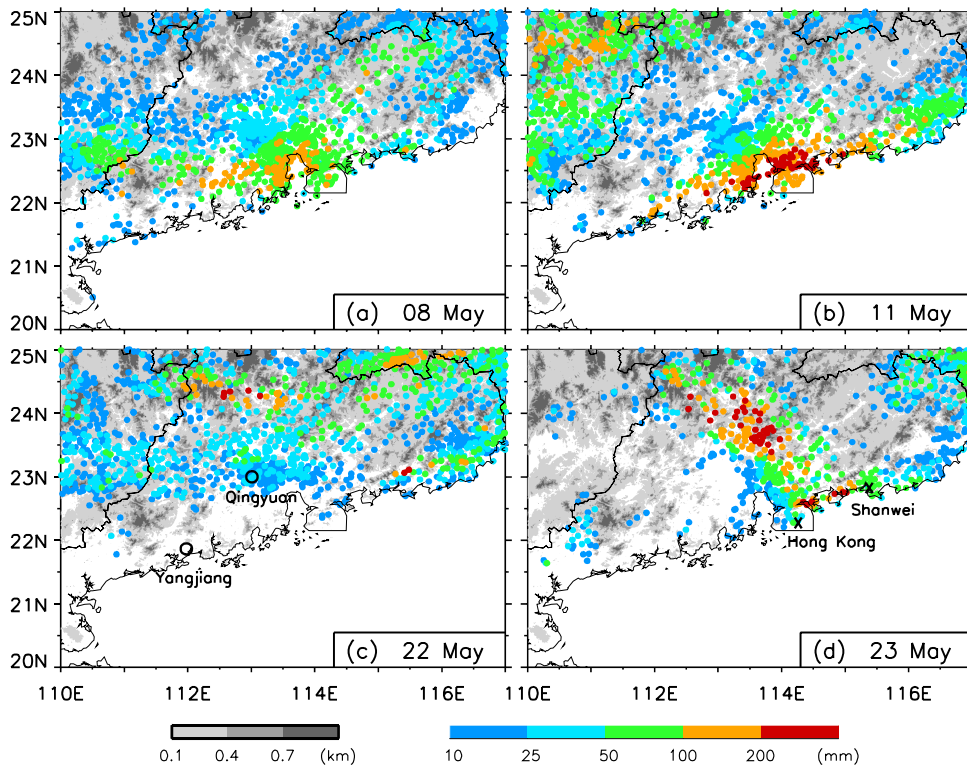


716  
 717

718 Figure 3 Time series of the number of rain gauges in Guangdong province within the  
 719 SCMREX enhanced observing area (orange rectangle lines in Fig. 2b) that  
 720 recorded extremely daily rainfall ( $>200 \text{ mm day}^{-1}$ , red lines;  $>100 \text{ mm day}^{-1}$ ,  
 721 blue lines) and heavy hourly rainfall ( $>20 \text{ mm h}^{-1}$ , grey bars) during (a) 2013, (b)  
 722 2014, and (c) 2015 IOPs. The total number of rain gauges was 1269 within the  
 723 analysis area.



725



726

727

728 Figure 4 Distribution of daily (0000 – 0000 BST) rainfall (mm) over the SCMREX

729 enhanced observing area (orange rectangle lines in Fig. 2a) on (a)–(d) 8, 11, 22,

730 and 23 May 2014. Gray shadings represent topography. The black circles in (c)

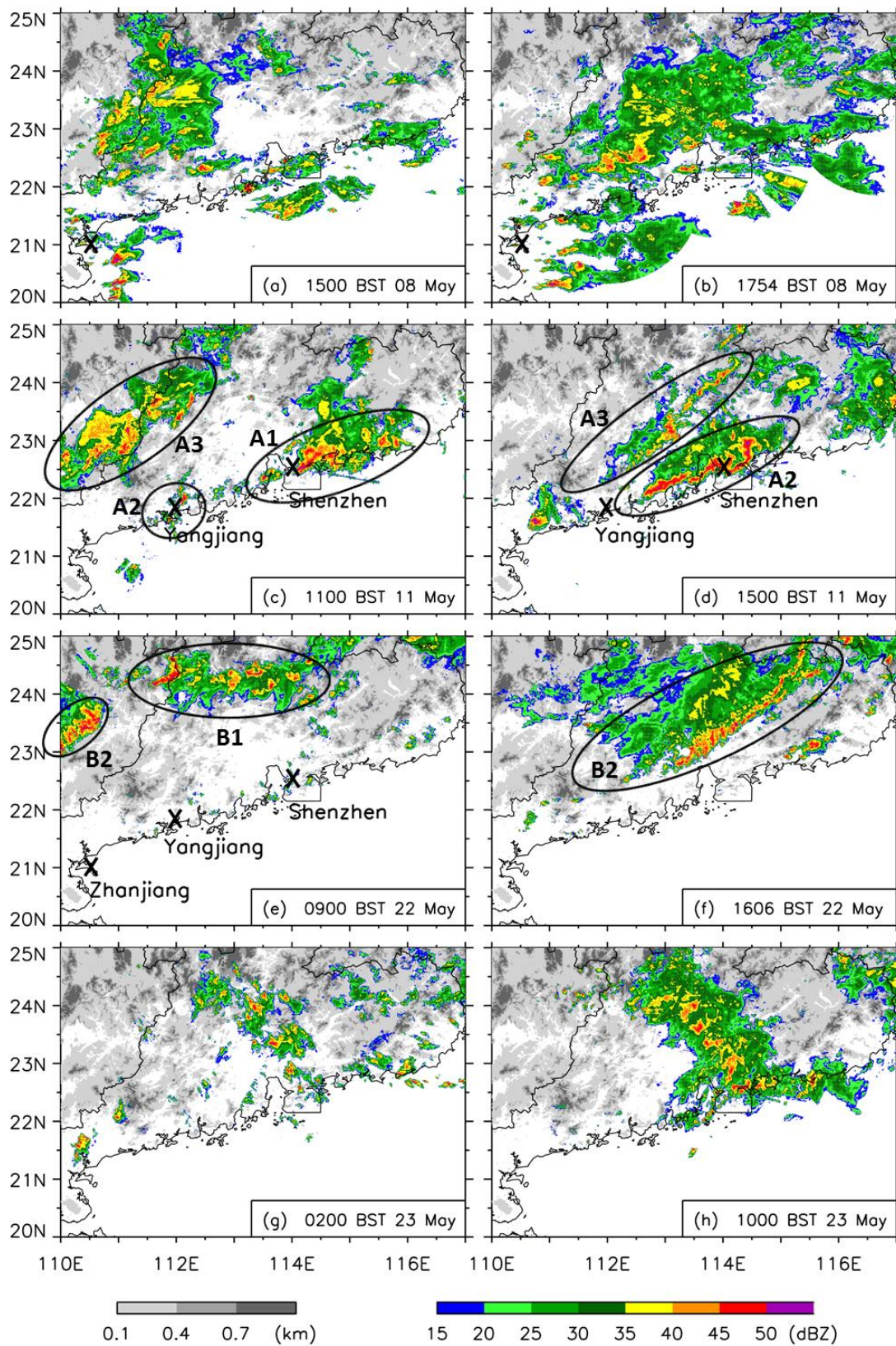
731 denote the locations of the sounding stations at Qingyuan and Yangjiang, while

732 the black crosses in (d) denote the locations of the operational S-band radars at

733 Hong Kong and Shanwei.

734

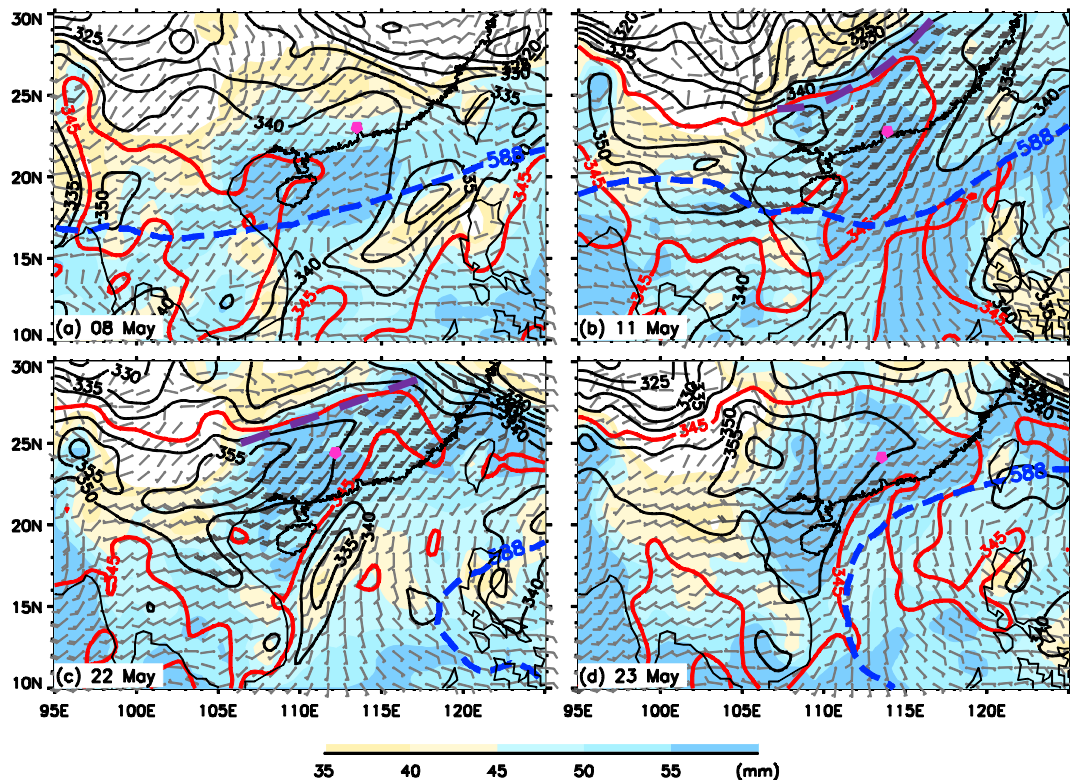
735



736

737 Figure 5 Radar reflectivity at 3-km altitude ASL in the enhanced observing area  
 738 (orange rectangle lines in Fig. 2a) derived from nine operational weather radars (8 in  
 739 Guangdong and 1 in east Guangxi) at two selected times on (a, b) 08 May, (c, d) 11

740 May, (e, f) 22 May, and (g, h) 23 May 2014, respectively. Gray shadings represent  
741 topography. The black crosses denote the locations of the operational S-band radars at  
742 Zhanjiang, Yangjiang, and Shenzhen, respectively. Ellipses in (c, d) and (e, f) denote  
743 the individual MCSs on 11 May and 22 May, respectively



744

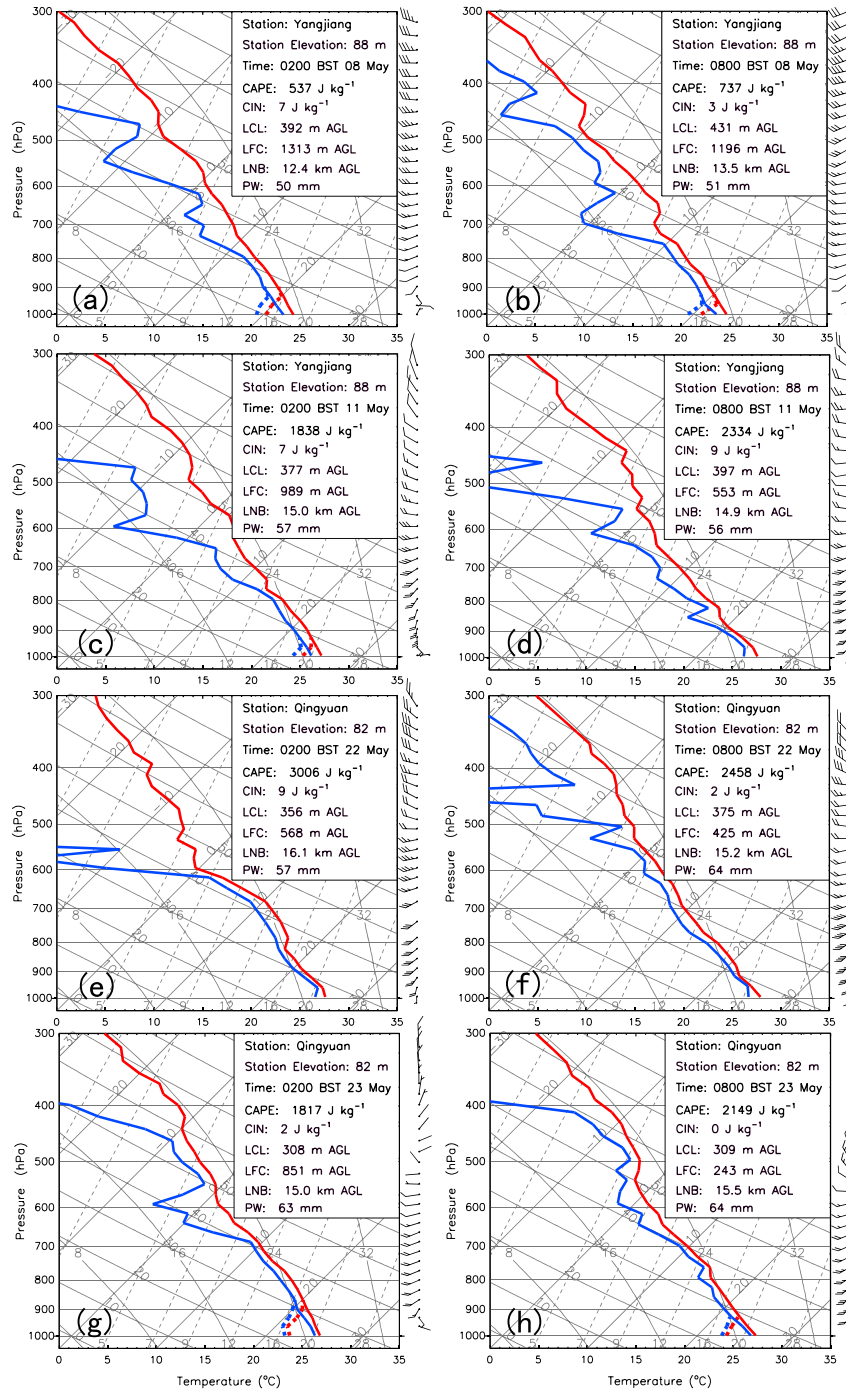
745 Figure 6 The ERA-interim analysis of 850 hPa at 0800 BST (a) 8 May, (b) 11 May, (c)  
 746 22 May, and (d) 23 May, 2014, showing the equivalent potential temperature ( $\theta_e$ ,  
 747 contoured at intervals of 5 K, with the 345 K contour in red) superimposed with  
 748 horizontal wind barbs, and also precipitable water (mm, shaded). A full barb is 5  
 749  $\text{m s}^{-1}$ . Shear lines at 850 hPa are shown by thick purple lines. The 588 dgpm  
 750 contours of the geopotential height at 500 hPa are denoted by blue dashed lines.  
 751 Pink stars denote locations of the heavy rainfall of interest on the corresponding  
 752 days.

753

754

755

756



757

758 Figure 7 (a)-(d) Skew T-log  $P$  diagram at Yangjiang sounding station (59663) at 02

759 BST and 08 BST on (a, b) 8 May and (c, d) 11 May. (e)-(h) As (a)-(d), but for

760 Qingyuan sounding station (59280) on (e, f) 22 May and (g, h) 23 May 2014. The

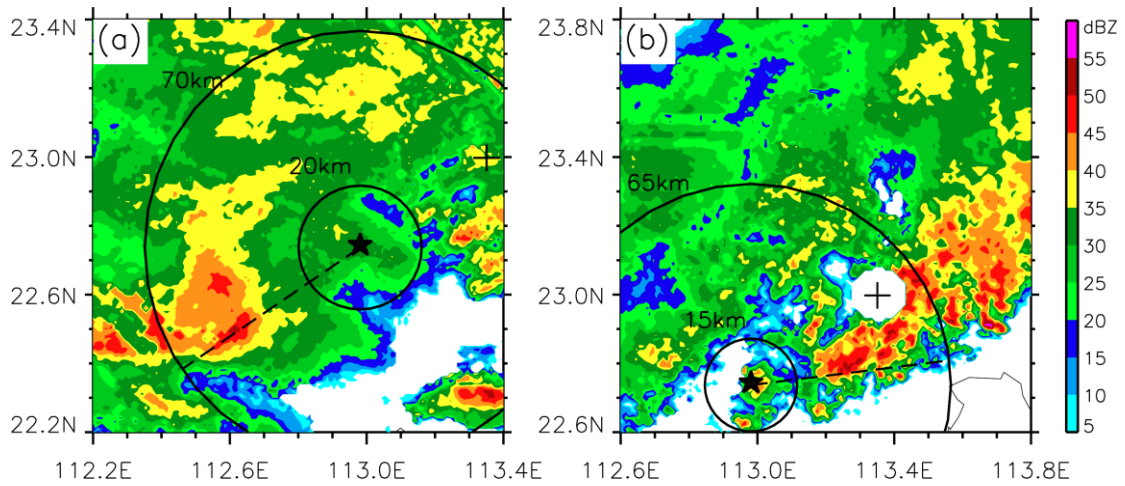
761 soundings on 8 May, at 02 BST of 11 May, and on 23 May were influenced by rain

762 evaporative cooling near the surface and corrected based on the observations from the

763 surface AWSs around the sounding station. The original soundings without the

764 correction are shown in the panels as short dashed lines, while the corrected

765 soundings are shown as solid lines. The values of CAPE, CIN, LCL, LFC, and LNB  
766 were calculated for the mass-weighted near surface air (0-500 m) after the correction.  
767  
768  
769  
770

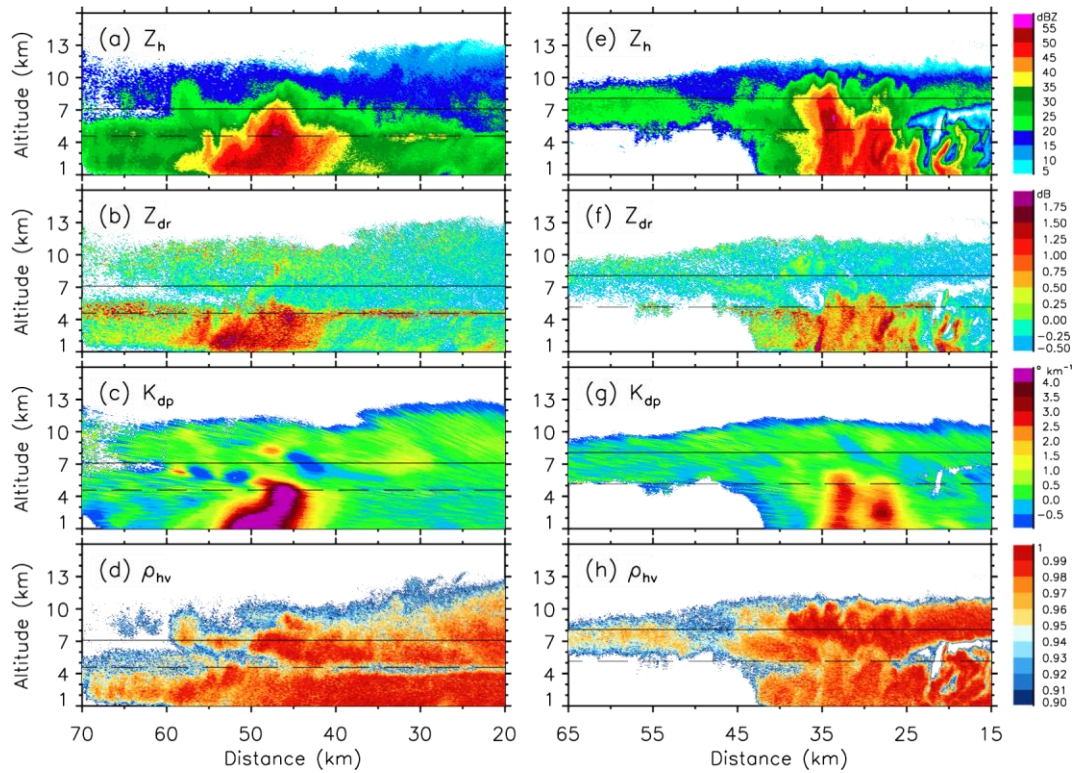


771

772

773 Figure 8 CAPPI at 3 km ASL derived from the Guangzhou S-band radar volumetric  
 774 scans at about (a) 1754 BST 8 May and (b) 1606 BST 22 May 2014. Cross and star  
 775 denote locations of the Guangzhou radar and the Heshan C-POL radar, respectively.  
 776 Black dashed lines represent the locations of the vertical cross sections to be shown in  
 777 Fig. 9.

778



779

780

781 Figure 9 (a)-(d) Vertical cross section at about 1752 BST 8 May of the Heshan C-POL

782 measurements of (a) reflectivity (dBZ), (b) differential reflectivity ( $Z_{dr}$ ), (c) specific

783 differential phase ( $K_{dp}$ ), and (d) correlation coefficient ( $\rho_{hv}$ ). The black dashed and

784 solid lines represent the  $0^{\circ}\text{C}$  level (4.6 km) and  $-15^{\circ}\text{C}$  level (7 km), respectively,

785 according to sounding data. (e)-(h) As in (a)-(d), but at about 1604 BST 22 May 2014

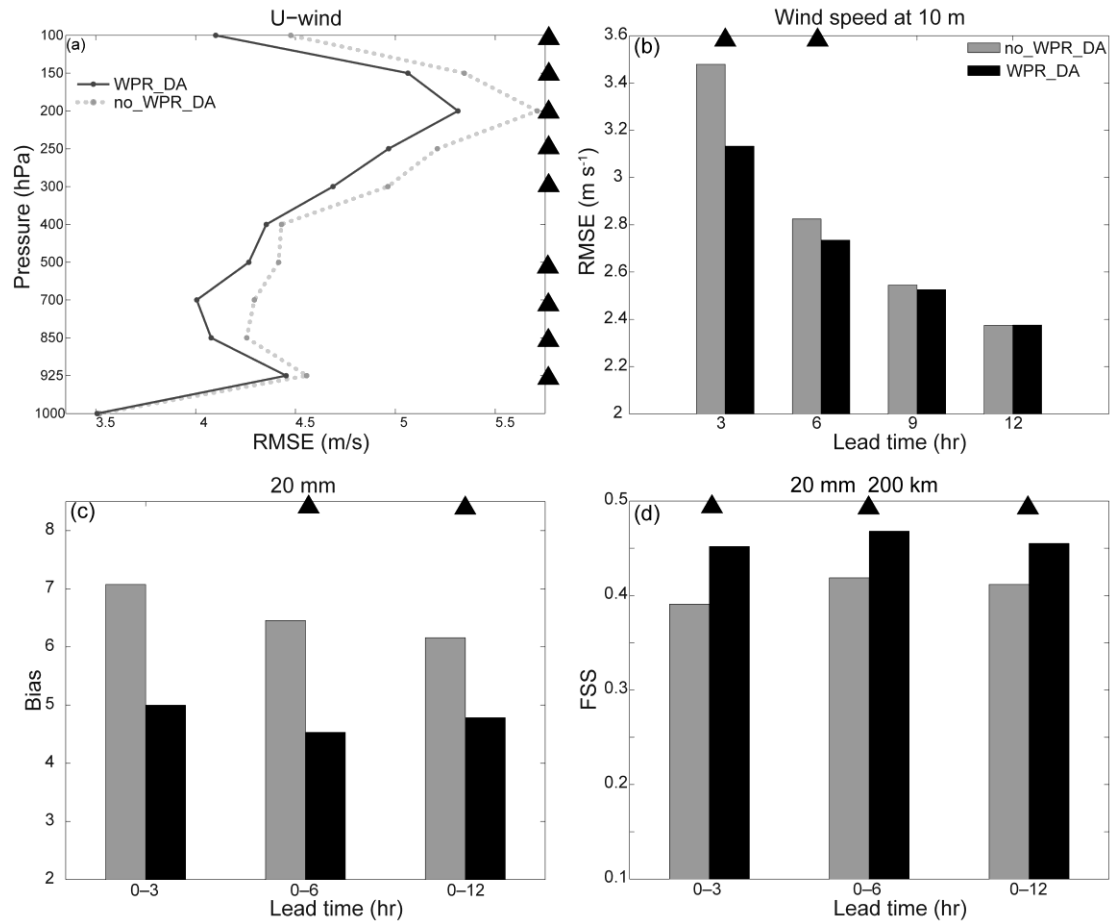
786 and the  $0^{\circ}\text{C}$  ( $-15^{\circ}\text{C}$ ) level is 5.2 km (8.1km).

787

788

789

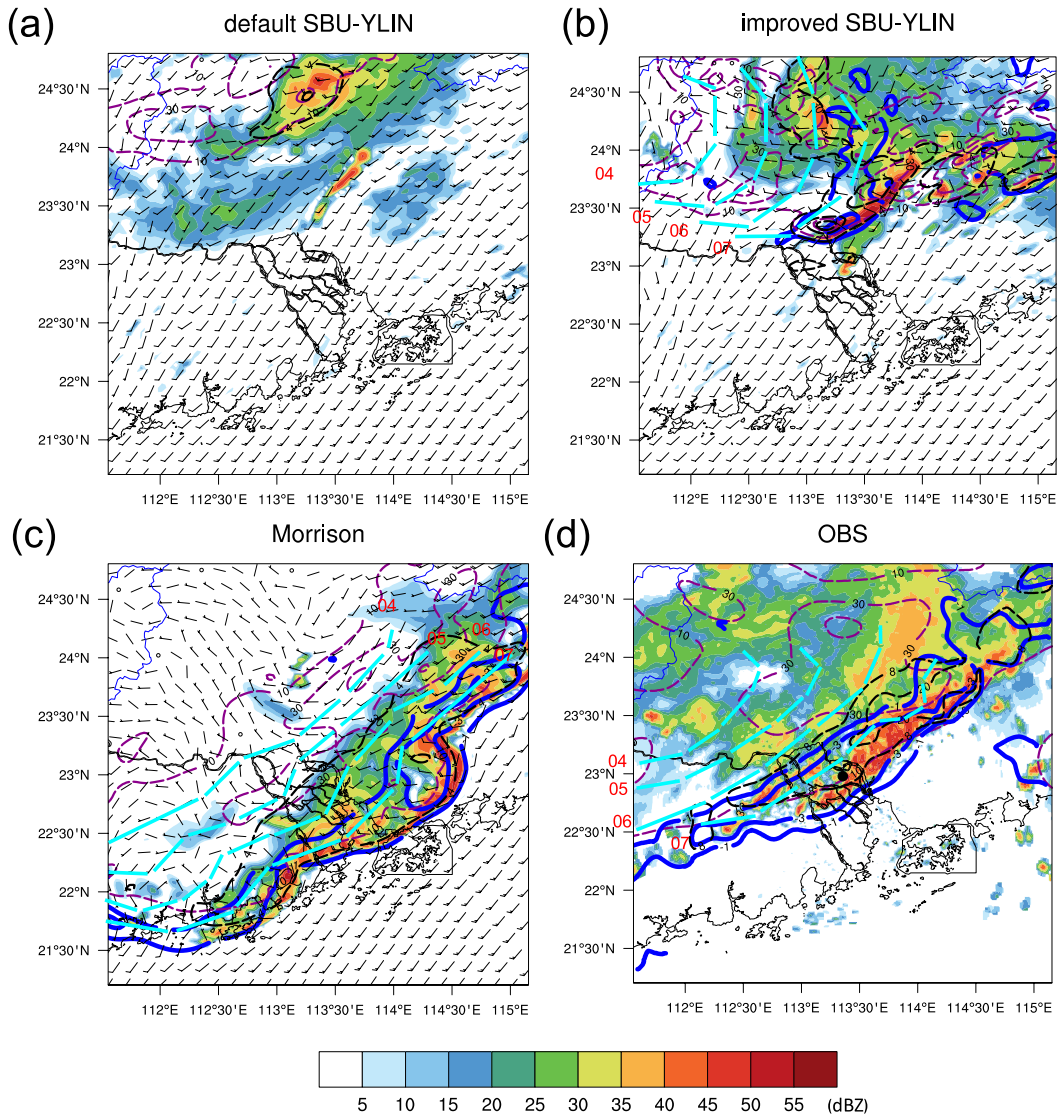
790



791

792 Figure 10 (a) Vertical profiles of root mean square errors (RMSEs) of the 12-h  
 793 forecasts of U-wind with respect to radiosonde observations in the two monthly  
 794 continuous experiments with (WPR\_DA; solid lines) and without (no\_WPR\_DA;  
 795 dotted lines), respectively, the WPR measurements being assimilated. (b) RMSEs  
 796 for the forecasts of horizontal wind speed at 10 m altitude AGL with respect to  
 797 surface observations in no\_WPR\_DA (light bars) and WPR\_DA (dark bars) as a  
 798 function of lead time. (c) Bias for the forecasts of 1-h accumulated precipitation (>  
 799 20 mm) averaged over different lead times in no\_WPR\_DA (gray bars) and  
 800 WPR\_DA (dark bars). (d) Fractions skill score (FSS) for the forecasts of 1-h  
 801 accumulated precipitation averaged over different lead times with precipitation  
 802 threshold of 20 mm and neighborhood length of 200 km in no\_WPR\_DA (gray  
 803 bars) and WPR\_DA (dark bars). Dark triangles indicate that the significance  
 804 level of the difference of (a, b) RMSE, (c) bias, and (d) FSS between WPR\_DA  
 805 and no\_WPR\_DA is greater than 90%.

806



808

809

810 Figure 11 Radar reflectivity (dBZ; color shaded) and wind barbs at 0.5 km ASL at  
 811 0800 UTC 22 May 2014, the 0400-0800 UTC total precipitation (mm; magenta  
 812 dashed lines), surface air temperature changes from 0700UTC to 0800UTC (K per  
 813 hour; blue solid lines), hourly precipitation ending at 0800 UTC (mm; black dashed  
 814 lines), and the location of the squall line during the previous 4 hours (cyan dashed  
 815 lines with red number denoting the time) from simulations using (a) the default  
 816 SBU-YLIN scheme, (b) the improved SBU-YLIN scheme, (c) the Morrison scheme  
 817 (c), and (d) from the observations except for without the wind barbs. The area covered  
 818 by the  $-3 \text{ K h}^{-1}$  contour of surface cooling rate is approximately an indication of the  
 819 cold pool. The black dot in (d) depicts the location of the Guangzhou radar.